Scanned conical illumination as a probe of electro-optic retro-reflection

Ali S. Alshomrany,[1,2] **Z. Nguyen,**[1] **Joseph E. Maclennan,**[1] **and Noel A. Clark**[1,*]

[1]*Department of Physics and Soft Materials Research Center, University of Colorado, Boulder, CO 80309, USA*
[2]*Department of Physics, College of Applied Sciences, Umm Al-Qura University, Mecca 24381, Saudi Arabia*
*noel.clark@colorado.edu

Abstract: We describe a prototype element for use in probing electro-optic retro-reflection in sensor applications, illuminating a planar-aligned nematic liquid crystal electro-optic cell with convergent light having a single, tunable angle of incidence (tunable conical illumination). This illumination is generated using a 100X, high numerical aperture, long working-distance microscope objective under conditions of extreme spherical aberration. The electro-optic effect observed is multiple-beam optical interference between polarized reflections from the two bounding plates of the cell, rendered tunable with voltage-controlled refractive index changes induced by molecular reorientation of the liquid crystal. Characterization of the reflectivity vs. angle of incidence and applied voltage enables identification of conditions of high-contrast, low power, electro-optic reflectivity control applicable to fiber optics.

1. Introduction

A variety of remote sensing applications are enabled by miniature optical sensing devices that generally report spectral changes in absorption or fluorescence and are interrogated at long range by retro-reflected laser light, delivered by fiber optic [1–4] or free space propagation [5–19]. The addition, to these and other remote devices, of a capability to communicate local information by intensity or phase modulation of the retro-reflected light would enable a variety of significant enhancements [20–22]. The implementation of such dynamic retro-reflection in such applications would benefit from high speed, low power, electro-optic methods that can give high contrast modulation of reflected light. Liquid crystal (LC) electro-optic (EO) devices, the basis of the light valves comprising the displays of laptops, pads, and phones, are a promising choice for dynamic retro-reflection applications. Although LC EO devices are of only moderate speed (millisecond to microsecond EO response times), their inherently low power consumption, diverse variety of EO effects, success as a commercial light valve technology, and potential for modulating obliquely incident light, make them attractive for sensing applications [23–26].

Efficient exploration of the EO effects that might be useful in such applications will require techniques whereby the inherently broad range of geometries and conditions available in LC devices, due to their flexibility of alignment, diversity of optical characteristics, and distinctive electro-optic effects, can be effectively probed. Here we present a method in which the reflection characteristics of an LC electro-optic cell, a geometry having a nematic LC layer as a few microns thick, dielectric film in a transparent capacitor, can be conveniently explored as a function of angle of incidence, polarization, applied voltage, and cell geometry. We describe a prototype element for use in probing electro-optic retro-reflection in sensor applications, illuminating a planar-aligned nematic liquid crystal electro-optic cell with convergent light having a single, tunable angle of incidence (tunable conical illumination), generated using a 100X, high numerical aperture, long working-distance microscope

objective under conditions of extreme spherical aberration. The electro-optic effect observed is multiple-beam optical interference between polarized reflections from the two bounding plates of the cell, rendered tunable with voltage-controlled refractive index changes induced by molecular reorientation of the liquid crystal.

This geometry would be suitable for information transfer from a sensing device that communicates using light incident from an optical fiber by modulating its reflection back down the fiber. The results show that the electro-optic contrast obtained depends strongly on angle of incidence, cell geometry and thickness, and LC parameters, and enable the design of high-contrast, low power, electro-optic reflectivity control applicable to fiber optics.

2. Experimental geometry

This method is based on a remarkable capability of advanced, infinity-corrected, high performance microscope objectives, afforded to them by the combination of high magnification, long working distance, and large numerical aperture. Specifically, if such a lens is designed to focus incident collimated light to a single point in air but is positioned such that the focal point would be inside a glass plate oriented normal to the objective axis, then a series of on-axis focal points appear, their position varying with the angle of incidence in air, θ_a, according to the rules of geometrical optics as applied to spherical aberration. If a second surface is introduced at the location of one of these focal points, then we find that the incident light is reflected back through the lens to the field center at infinity in the form of nearly perfect conical reflection, the cone having the angle of incidence corresponding precisely to the calculated spherical aberration at the second surface location. This is a simple geometrical optics result but the high performance of advanced objectives enables it to be achieved with precision and single-degree angular resolution, such that scans of incident angle can be made via z-scans of the objective position, as discussed below.

The basic test setup, shown in Fig. 1, has a collimated 632.8 nm laser beam focused by an infinity-corrected 100X microscope objective (NA = 0.8) onto various optical geometries, with the reflected light collected effectively at infinity by a distant, small area (2 mm^2), amplified Si detector, D2. The objective employed (Olympus LMPlanFlI [27], NA = 0.8) is engineered for imaging at the air/sample interface, producing a diffraction limited focus of the incident beam in air (Fig. 1). Measurement of the intensity at D2 during positional scanning of the objective parallel to the beam (z-scanning, Fig. 2(a)) provides a measurement of the normalized reflected intensity $N(z)$, and an indication of the depth of focus of the diffraction-limited beam, as shown in Fig. 2(b). The focal peak is found to be characterized by a full width at a half height in z of $\Delta z_{FWHH} = 1.62$ µm, which is the diffraction-limited depth of focus for this objective for a plane wave uniformly illuminating its aperture.

3. Conical illumination

Useful LC electro-optic geometries require the liquid crystal material to be between solid plates, enabling alignment of the LC and the application of electric fields, in which case the probe light must pass through some thickness of glass or other transparent optical material. If an objective corrected to focus in air as in Fig. 1 is used, then its behavior when focusing through glass will be affected by aberration, as illustrated in Fig. 2. Aberration produces classic features of a degraded focus, including an asymmetric distribution of on-axis intensity that is much broader (Fig. 2(h)) than that of the aberration-free focus (Fig. 2(b)).

The geometrical optics description of this ascribes the aberration to the nonlinearities inherent in Snell's law, which will cause the rays perfectly focused in air to intersect the system axis in glass at distances increasingly further from the lens as the angle of incidence in air, θ_a, is increased. If z measures the distance between the first glass interface and the position of the focal spot if the glass were removed, then for an angle of incidence $\theta_a(z, t_g)$, the crossing point is a distance $t(z)$ into the glass. If the plate is of finite thickness, so that there is a second reflecting interface a distance t_g into the glass, and the crossing point is

constrained to be at this interface, (i.e., $t(z) = t_g$, as sketched in Fig. 2(e)), then incident collimated light at the angle of incidence $\theta_a(z, t_g)$, will produce reflected collimated light. The relationship between θ_a and the lens position z is described by Eq. (1):

$$\theta_a = \sin^{-1}\left[\sqrt{\frac{1-\left(\dfrac{n_g z}{n_a t_g}\right)^2}{1-\left(\dfrac{z}{t_g}\right)^2}}\right] \tag{1}$$
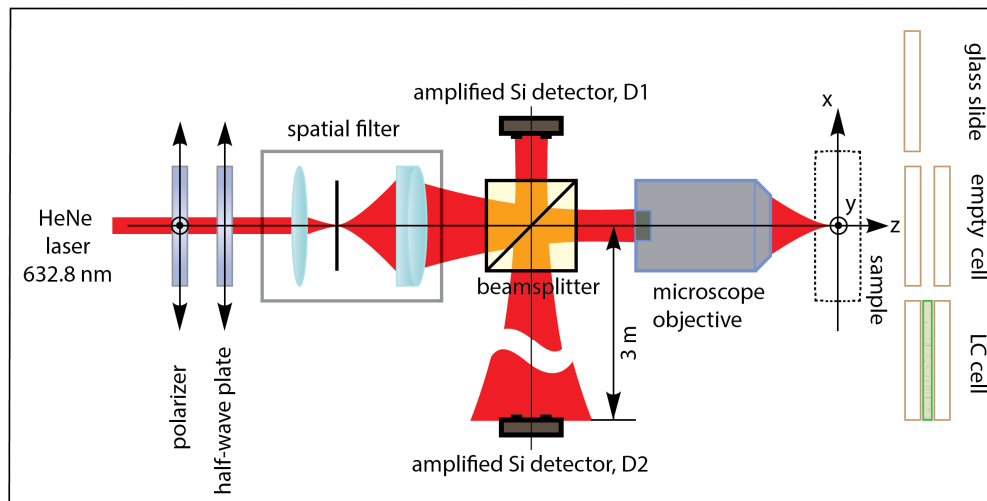

Fig. 1. Schematic diagram of the optical reflectometer. Monochromatic, linearly polarized light from a He-Ne laser is spatially filtered and collimated. A beam splitter divides the collimated light into two separate beams, one of which passes through a microscope objective designed to focus parallel light to a diffraction-limited focal spot in air, while the other is used as an intensity reference. The sample position along the beam axis (z) can be scanned using a motorized drive with 50 nm repeatability and precision. Light focused by the objective is reflected by the planar interfaces of the sample (oriented normal to z). The part of the reflection that passes back through the objective and is sufficiently parallel to the z axis is reflected by the beam splitter to a 3 m distant silicon photodiode D2. The approximate distance from the spatial filter to the beam splitter is 0.3 m, from the beam splitter to the objective 0.6 m, and from the beam splitter to D1 0.5 m. Detectors D1 and D2 both have 2 mm apertures. Three different sample types, a glass slide, an air-filled sandwich cell, and a transparent capacitor cell filled with liquid crystal, were studied.

As z is increased from z = 0, the first rays to be so reflected will be those for the largest θ_a, θ_{amax}, when $z = z(\theta_{amax})$, as in Fig. 2(d). As z is increased further, the θ_a for collimated reflection will decrease until $z = z(\theta_a = 0) = t_g/n_g$, where the on-axis rays focus (Fig. 2(f)). Figure 2(g) shows $\theta_a(z)$ vs. z calculated using Eq. (1), for the range of θ_a corresponding to our objective. Figures 2(h) and 3(a) show $N_{glass}(z)$, the corresponding collimated reflected intensity from the glass collected at detector D2, normalized such that the front surface reflection has unit peak intensity, i.e., N(z = 0) = 1. The aberrated reflected intensity is largest near $\theta_a = 0$, where the small-angle rays focus, and becomes smaller with decreasing z until θ_a $\sim\theta_{amax}$, beyond which angle the light is cut off by the objective aperture [28–32]. Also shown in Fig. 3(a) are N(z) for the same glass plate with either indium tin oxide (ITO) or ITO coated with polyimide (PI) on the back interface. Since these are of thickness much smaller than the wavelength ($t_{ITO} = 44$ nm and $t_{PI} = 17$ nm), their reflectivities differ from that of the glass only by a θ_a-independent factor. Fringes that appear in $N_{glass}(z)$ for small θ_a, shown in Figs. 2(h) and 3(a), are a result of the modulation of the field amplitude of the focused light by edge

diffraction along the caustic curve evident in the converging light in Fig. 2(i). The intersection of this conical fringe pattern with the lens axis generates the quasi-periodic intensity modulation in N(z) [33–38].
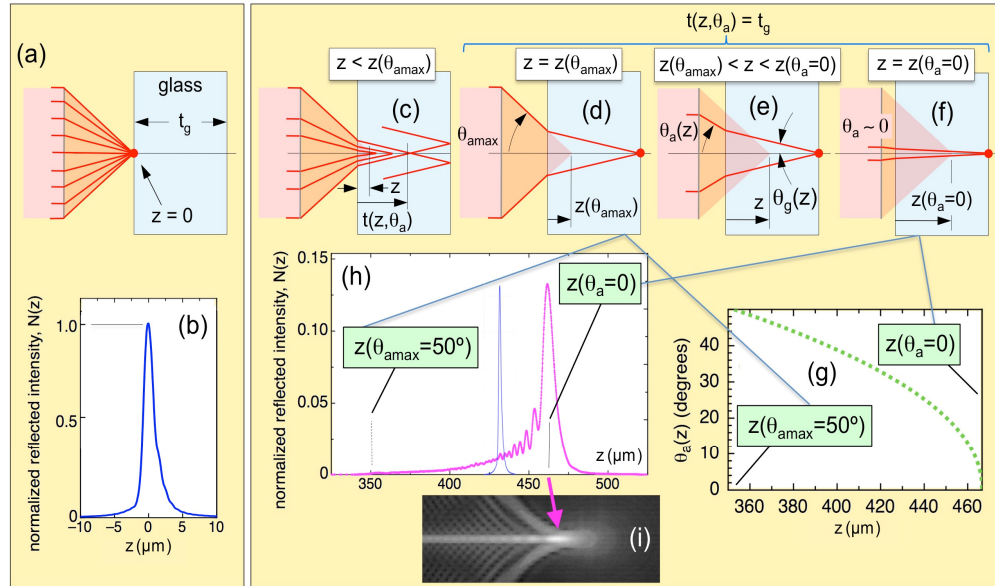

Fig. 2. Snapshots of the geometry and the notation used to describe the axial z-scan of the focal spot through a slab of dielectric (a glass slide), where z gives the relative position of the objective and sample. (a) The scan through $z = 0$, where the air-glass interface lies in the plane of the unaberrated, diffraction-limited focus of the objective gives (b) a sharp, single reflection peak at z = 0. (c) For $z > 0$, spherical aberration causes the focal distance in the glass plate to depend on the angle of incidence θ_a, with the rays with larger θ_a focusing further into the glass. (d) As the slide is scanned through $z = 350$ μm, where the aberrated focal plane of the (peripheral) ray of largest θ_a intersects the planar back face of the glass, reflected intensity begins to be detected at D2. (e) As z is increased further, the value of θ_a producing a back-face reflection at D2 decreases, until (f) at $z(\theta_a = 0)$, on-axis rays are reflected. (h) In the range of θ_a between (d) and (f), a broad reflection band of intensity [magenta curve, plotted with the same vertical scale as 2(b)] with a distinctive modulated structure, a maximum near $\theta_a = 0$ where spherical aberration is minimum, and an exponential tail toward increasing θ_a, is observed at D2. This reflected intensity distribution is significantly broadened, as can be seen by comparing it with the aberration-free front surface reflection [blue, from (b) but here scaled to the magenta peak value], but is very similar to (i) an intensity distribution of focused, aberrated light field for a geometry comparable to ours ($n_g = 1.55$ and NA = 0.9), obtained using the diffraction integral representation [34]. (g) Computed angular dependence of θ_a on z for $n_{glass} = 1.55$.

Multiple beam interference as a probe of conical illumination

A diffraction integral calculation of the on-axis intensity $I(z)$ in a geometry of spherical aberration very similar to ours ($n_g = 1.55$, NA = 0.9 [39–41]) is shown in Fig. 3(b). The similarity of the calculated $I(z)$ and $N_{glass}(z)$ suggests that the measurement of $N_{glass}(z)$ may be an effective way to probe $I(z)$. In order to test this proposition, and as a prelude to the study of liquid crystal cells, we introduced a third interface to make an air-filled cell of thickness t_{cell} ≈4.5 μm, sketched in Fig. 4. This cell becomes a low finesse, multiple beam interferometer with a path difference for interference that depends on $\theta_g = (1/n_g) \sin\theta_a$, the angle of incidence in the glass (Fig. 2(e)). $N_{cell}(z)$ measured for this air gap cell, plotted along with $N_{glass}(z)$ in Fig. 3(c), shows distinctive interference minima for z in the range 350 μm $< z <$ 470 μm, corresponding to θ_a in the range 50° $> \theta_a >$ 0°. The reflected intensity ratio $R_{cell}(z) = N_{cell}(z)/N_{glass}(z)$, plotted in Fig. 3(d), exhibits the following features: (i) constructive

interference maxima of $R(z) \approx 4$ for $\theta_a < 50°$; (ii) destructive interference minima of $R(z)$ ~0.05 for $\theta_a < 50°$; (iii) reflection without interference from two glass surfaces giving R ~2 for $z > 470$ μm, where focus is not possible.

For obliquely incident, parallel, monochromatic light, this air gap cell should have a reflected intensity ratio $R_{cell}(\theta_a, n_a, n_g, t_{cell}, \delta, z)$ given by the intensity reflectivity interference function of the cell, $r^2_{cell} = r^2_{gap}$, divided by the glass/air Fresnel reflectivity, $r^2_{g/a}$,

$$R_{cell}(\theta_a, n_a, n_g, t_g, \delta_{gap}, z) = \frac{r^2_{gap}}{r^2_{g/a}} = \frac{2(1 - \cos 2\delta_{gap})}{r^2_{g/a}(r^2_{g/a} - 2\cos 2\delta_{gap}) + 1}. \tag{2}$$

where $r(\theta_a)$ is the glass/air Fresnel amplitude reflection coefficient, and δ_{gap} is the optical phase difference given by

$$\delta_{gap} = 2\pi m \tag{3}$$

Here m is the interference order, which depends on the wavelength of the laser λ, the index of refraction n_{cell} of the gap, the thickness t_{cell} of the gap, and the scanning position z. For the phase change on reflection at oblique incidence through the gap, the general interference order is obtained from the relation

$$m = \frac{2n_{cell}t_{cell}}{\lambda} \sqrt{1 - \left(\frac{n_a}{n_{cell}}\right)^2 \left[\frac{1 - \left(\frac{n_g z}{n_a t_g}\right)^2}{1 - \left(\frac{z}{t_g}\right)^2}\right]} \tag{4}$$
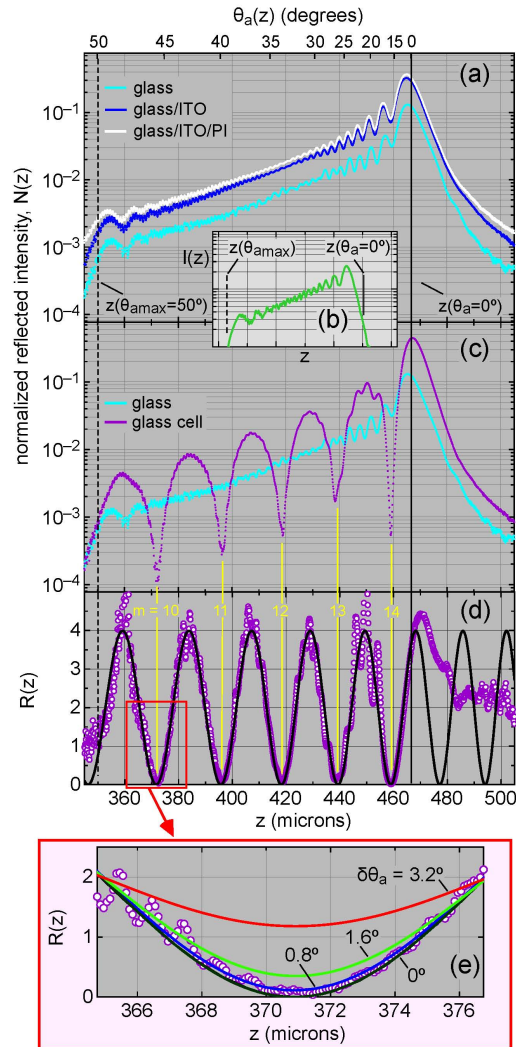
with the zeros in R_{cell} occurring for integer values of m.

Fig. 3. (a) Normalized retro-reflectivity $N_{glass}(z)$ of a single, uncoated glass slide (t_g = 724 µm, n_g = 1.55), and of similar plates coated with ITO and PI on the back side as indicated. The coatings substantially change the magnitude of $N(z)$, but not the overall shape. (b) On-axis intensity $I(z)$ vs. position z, calculated using the diffraction integral representation for a focusing geometry comparable to ours (n_g = 1.55 and NA = 0.9 [34]). Comparison with (a) indicates that $N(z)$ is proportional to the on-axis intensity at the reflecting interface. (c) Normalized retro-reflection $N_{cell}(z)$ for a t_{cell} = 4.5 µm glass air-gap cell, plotted along with $N_{glass}(z)$, showing the interference effect of multiple reflections between the back and front interfaces of the air gap. At conditions of constructive interference, we see that $N_{cell}(z)/N_{glass}(z)$ ≈4, and for $z > z(\theta_a = 0)$, where there is no longer interference, $N_{cell}(z)/N_{glass}(z)$ ≈2, the expected result for incoherent reflection from two surfaces. (d) Plot of $R(z) = N_{cell}(z)/N_{glass}(z)$ fitted by the interference function, $R_{cell}(z)$ of Eq. (4). (e) Fit to $R_{cell}(z)$ in the vicinity of the extinction minimum at m = 10, convolved with a flat-topped distribution of width $\delta\theta_a$, showing that the angular width of the cone of light selected in the retro-reflection geometry is very narrow: $\delta\theta_a$ ~0.8° at θ_a = 45°.
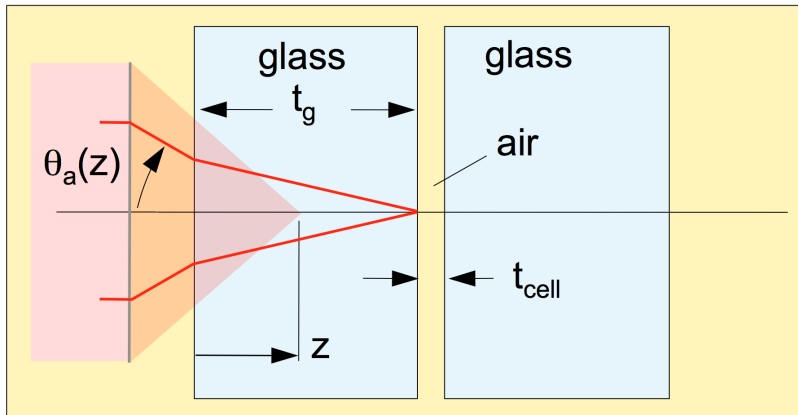
Fig. 4. Schematic showing retro-reflection from an air-gap cell. The front glass plate has a thickness t_g and the air gap is t_{cell}. θ_a is the angle of incidence of the light ray on entering the glass.

The black curve in Fig. 3(d) is a least-squares fit of Eq. (2) to $R_{cell}(\theta_a)$, showing that this basic interference function depending on a single selected angle of incidence fits the data well in the range of z where there is focus of some selected ray at $\theta_a(z)$. That is, it appears that $\Delta\theta_a(z)$, the range of angles of incidence selected in the aberrated focus at $\theta_a(z)$ by the detection of collimated reflected far-field light, is much narrower that the θ_a range corresponding to that of the fringe spacing. The effective range of angles selected $\delta\theta_{am}$ in the vicinity of interference minimum m can be probed quantitatively by comparing the $R_{cell}(z)$ data of Figs. 3(c) and 3(d) in the vicinity of the minimum to a model in which there is a distribution of incident angles about $\theta_a(z)$. For this purpose we performed convolutions of the reflectivity $R_{cell}(\theta_a)$ calculated using Eq. (2) with the flat-topped distribution: $D(\theta_a) = 1/\delta\theta_a$ for $-\delta\theta_a/2 < \theta_a < \delta\theta_a/2$, $D(\theta_a) = 0$ for $\theta_a < -\delta\theta_a/2$ and $\theta_a > \delta\theta_a/2$. Sample convolutions $R(\theta_a) \otimes D(\theta_a)$ in the vicinity of the $m = 10$ minimum are shown in Fig. 3(e) for several $\delta\theta_a$ values, along with the measured extinction. A least squares fit of the convolution to the $m = 10$ data (black curve) gives $\delta\theta_a = 0.8°$. This value shows that the angular selection of cone angle of illumination in the retro-reflection of aberrated light using the Olympus 100X objective is quite narrow, making the variation of z an effective way of tuning cone angle.

The reflectivity data of Fig. 3(c,d) and the fit $R_{cell}(\theta_a)$ are shown again in Fig. 5(b), along with Fig. 5(a), a plot of Eq. (4) giving the dependence of the interference order m on z, n_{cell}, and t_{cell}, enabling the determination of $m(0) \equiv m(\theta_a = 0)$. For the air gap cell, $t_{cell} \approx 4.5$ μm and $n_{cell} = 1$ gives $m(0) = 14.6$, and minima in θ_a in the range $50° > \theta_a > 0°$ for $m = 10, 11, 12, 13$, and 14, as indicated by the construction of violet lines and violet/white open circles in Figs. 5(a) and 5(b).

4. Liquid crystal electro-optic reflection

The aberrated illumination geometry described in the previous section was applied to the investigation of the retro-reflection characteristics of planar-aligned nematic liquid crystal electro-optic cells, in the geometry shown in Figs. 6(a) and 6(b). The liquid crystal 5CB, a room temperature nematic with uniaxial extraordinary and ordinary refractive indices $n_e = 1.72$ and $n_o = 1.54$, was introduced into cells, custom made by Instec, Inc., comprising two glass plates spaced by a $t_{cell} \approx 4.5$ μm gap and coated on the gap faces with ITO electrodes as described above, to make a transparent capacitor with the LC as the dielectric. The electrodes were coated with a rubbed Nissan polyimide layer to generate planar-alignment with the nematic director $n(r)$, the local average mean molecular long axis orientation in the cell, approximately parallel to the plane of the gap surfaces and to the incident optical polarization, as shown in Fig. 6(b). Rubbing of the PI films orients n at the surface along the rubbing

direction with a pretilt angle of 5° relative to the surface (Instec specification). Antiparallel rubbing of the two cell plates then gives a uniform director orientation in the cell with $\psi(\mathbf{r})$ ≈5°, where $\psi(\mathbf{r})$ is the angle between $\mathbf{n}(\mathbf{r})$ and the x-y plane. Application of an AC voltage (peak-to-peak amplitude, v) across the cell produces a torque on $\mathbf{n}$ due to the dielectric anisotropy of the LC, inducing an increase in $\psi(\mathbf{r})$ throughout the cell. Since the cell is homogeneous in the x-y plane, the director orientation with a field applied depends only on s, the distance into the LC from the front cell surface. At high voltage, the orientation of $\mathbf{n}$ is nearly along the applied electric field, normal to the cell plates ($\psi(s)$ ≈90° with $v = 6$V). The orientation in the cell center, $\psi_c = \psi(s = t_{cell}/2)$, is obtained from Frank elastic energy calculations of the director distortion vs. applied voltage [42,43] using the known parameters for 5CB [44]. The calculations show that the main optical response is in the angular mid-range where ψ_c is changing rapidly, as expected.
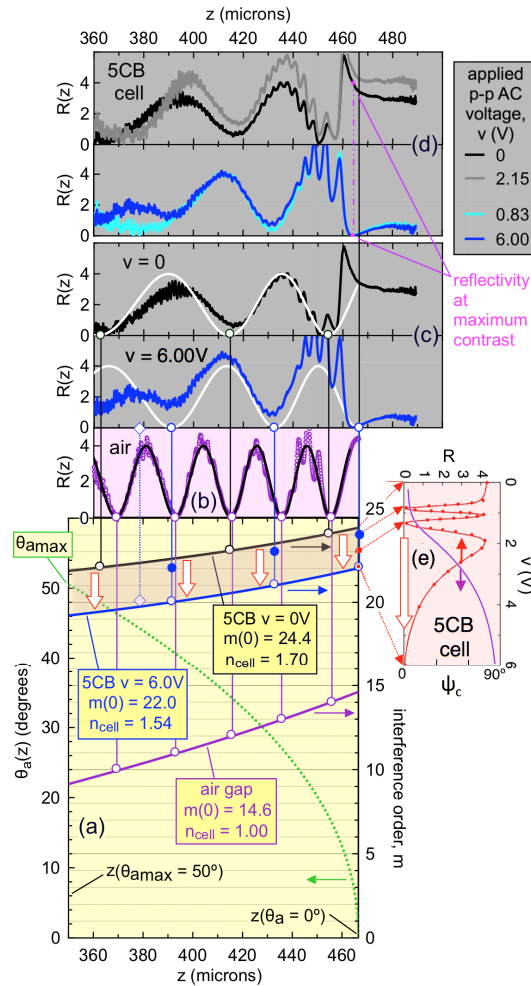
Fig. 5. (a) Graphical representation of the dependence of θ_a and of interference order, $m(\theta_a(z))$, on scan position, z. Here m is defined such that integral $m(\theta_a)$ corresponds to destructive interference and $m(\theta_a = 0) = (2n_{cell}t_{cell})/\lambda$. Also shown in (a) are $\theta_a(z)$ and $m(\theta_a)$ calculated for the three relevant cases of air gap (purple); 5CB LC gap with $v = 6.0$ V (homeotropic, $\psi \approx 90°$, blue); 5CB LC gap with $v = 0$ V (planar, $\psi \approx 90°$, black). (a,b) The extinctions (white circles) for the air gap case are projected up onto (b), which match accurately with air $N(z)$ data. (c) Black curve: $R_{0V}(z) = N_{0V}(z)/N_{coated}(z)$; blue curve: $R_{6V}(z)$; white curve: $R_{cell}(\theta_a(z))$ calculated from Eq. (2). The extinctions (white circles) for the 5CB LC gap cases are projected up onto (c), giving the minima for the white curves which, for $n_{cell} = n_e$ = 1.70 with $v = 0$ V and $n_{cell} = n_o = 1.54$ with $v = 6.0$ V, respectively match the $R_{0V}(z)$ and $R_{6V}(z)$ data well. (d) Comparison of the $v = 0$ V (black curve) and $v = 2.15$ V (yellow curve) cases. These both have half-integral order m at $\theta_a = 0$, and a principal optic axis nearly along z ($\psi \sim 0°$ and $m = 24.5$ with $v = 0$ V; $\psi \sim 90°$ and $m = 22.5$ with $v = 2.15$ V). Also shown is a comparison of the $v = 0.83$ V (black curve) and $v = 6.0$ V (yellow curve) cases. These both have integral order m at $\theta_a \approx 0$, and a principal optic axis nearly along z ($\psi \sim 0°$ and $m = 24$ with $v = 0.83$ V; $\psi \sim 90°$ and $m = 22$ with $v = 6.0$ V), providing a way to adjust n_{cell} and t_{cell} for maximum electro-optic contrast. (e) On-axis ($\theta_a = 0$) reflectivity vs. applied AC voltage, showing that the full voltage range scans m through 2.5 orders of multiple beam interference. The purple curve gives $\psi_c(v)$, the field-induced director tilt in the cell center which determines the effective refractive index of the liquid crystal layer.
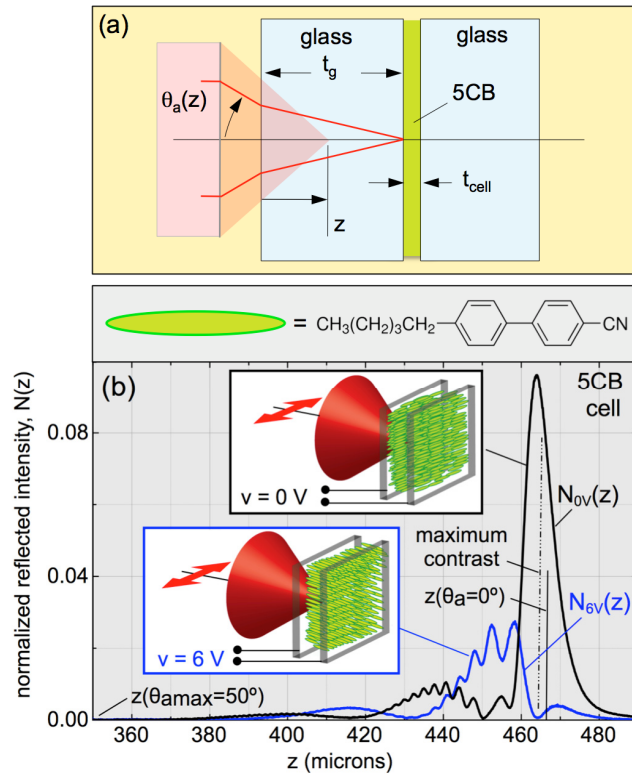
Fig. 6. (a) Liquid crystal electro-optic retro-reflector geometry, along with the structure of 5CB, the room-temperature nematic liquid crystal used. (b) Sketch of the planar-aligned LC cell with the average molecular long axis, *n*, parallel to the plates in the absence of applied field (*v* = 0) and normal to the glass plates in a large applied field (*v* = 6 V). Also shown are *z*-scan plots of normalized, retro-reflected intensity for incident polarization parallel to the zero-field orientation of *n*, when *v* = 0 V ($N_{0V}(z)$) and from the field-aligned cell with *v* = 6 V ($N_{6V}(z)$). These *N*(*z*) curves show multiple-beam interference fringes in the scan range $0° < \theta_a < 50°$. Maxima and minima of *N*(*z*) are observed at scan positions separated by $\Delta z \sim 50$ μm for which the path difference between light reflecting from the front and rear LC/cell interfaces satisfies constructive and destructive interference conditions, respectively. Cell conditions here are chosen such that a scanning position exists, in this case at *z* = 465 μm, where $N_{0V}(z)$ has a maximum reflection peak and $N_{6V}(z)$ has a destructive interference minimum, leading to the possibility of high-contrast voltage modulation of the intensity of the retro-reflected light near this *z*.

Normalized cell reflectivity *z*-scans *N*(*z*) obtained in the limits of planar orientation (*v* = 0V) and field-induced homeotropic orientation (*v* = 6 V), plotted in Fig. 6(b), confirm that *N*(*z*) depends strongly on applied voltage. At *v* = 0 V, the maximum of the reflectivity peak is *N*(*z* = 465 μm) ~0.1, which is much smaller than that which would be obtained from an empty (air gap) glass/ITO/PI cell (*N*(*z* = 465 μm) ~1) as shown in Fig. 3(c), a result of the reflectivity at the glass/ITO/PI – LC interface being much smaller than that of the glass/ITO/PI – air interface because of index matching. The incident light is polarized along *x*, parallel to the director orientation *n* in the absence of field. Applied electric fields rotate the director in the *x-z* plane, a plane of mirror symmetry of the cell. As a result, the light is not depolarized by the LC birefringence, remaining polarized on average parallel to *n*, and the electro-optic effect is due principally to variation of the effective refractive index due to the rotation of *n* and to the resulting changes in the multiple beam interference between reflections at the interior cell surfaces. The field dependence of the refractive index in the cell substantially controls the variation of *N*(*z*) with field, and, in particular produces strong variation of *N*(*z*) at certain values of *z*. For example, setting *z* ≈465 μm, near the reflectivity

maximum at $\theta_a = 0$, yields high contrast variation of $N(z)$ as interference minima in the vicinity are tuned through by varying the applied voltage v, as shown in Fig. 7(a). The field dependence was further explored by tracking the evolution of $N(z)$ vs. applied voltage in the full range of director orientation in the cell, from planar to saturated homeotropic, as shown in Fig. 7. At $v = 0$ V, $N(z)$ possesses a maximum reflection at position $z = 465$ μm corresponding to the nematic LC director $\boldsymbol{n}$ essentially parallel to the x-y plane and thus approximately parallel to the optical polarization of the incident conical beam. As v increases, the nematic LC director $\boldsymbol{n}$ reorients toward the field direction and generally away from the optical polarization direction, resulting in a decrease of the effective refractive index of the LC medium. The maximum contrast ratio of $N(z)$ was obtained at the peak position $z = 465$ μm, where applied voltage can tune the effective LC index to a value that gives extinction at both $v = 0.83$ V and $v = 6.00$ V. Interestingly, the high voltage regime, in the range 2.15 V $< v <$ 6.00 V, shows a variation in the interference patterns that is nearly identical to that obtained when the voltage is scanned in the 0 V $< v <$ 0.83 V low voltage regime, as seen by comparing Figs. 7(a) and 7(c).
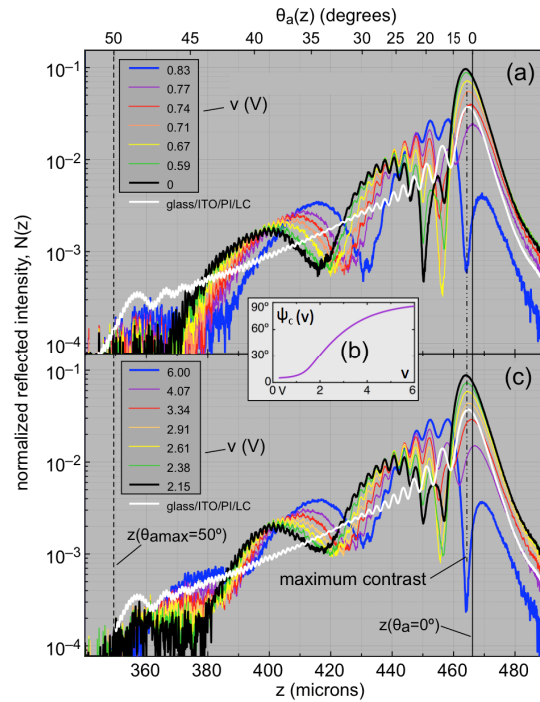

Fig. 7. (a,c) Multi-z-scan plot showing the interference patterns and their voltage dependence, $N_V(z)$, for the planar-aligned nematic LC 5CB cell with applied voltage in the ranges 0 V $< v <$ 0.83 V and 2.15 V $< v <$ 6.0 V. Also plotted is the coated plate reflectivity $N_{coated}(z)$ including the index matching effect of the LC at $v = 0$ V (white). The ratio $R(z) = N_V(z)/N_{coated}(z) \sim 4$ for constructive interference, as was the case for the air-gap cell. (b) Inset showing numerical calculation of $\psi(v)$, the field-induced rotation of $\boldsymbol{n}$ from planar alignment in the midplane of the cell as a function of applied voltage. Electro-optic response of $N_V(z)$ for increasing the applied peak-to-peak voltages from $v = 0$ V to $v = 0.83$ V, the regime where $\psi(v)$ is small. Increasing voltage produces a continuous shift in the interference minima toward smaller θ_a. (c) Electro-optic response of $N_V(z)$ for applied voltage amplitudes from $v = 2.15$ V to $v = 6.0$ V, the limit where $\psi(v) \sim 90°$. Increasing voltage produces a continuous shift in the interference minima toward smaller θ_a, a consequence of the concomitant effective reduction in refractive index of the LC layer. The dependence of $N_V(z)$ on v is very similar in (a) and (c) because a principal axis of the optical dielectric tensor is nearly along the normal to the cell plane, z, in both cases, and because the field-induced trajectory in $m(z)$ differs by the integral value $\delta m = 2$ between the two cases.

Voltage dependent reflectivity data $R(v,z)$ are compared to theoretical predictions for a variety of conical scans in Fig. 5. The lower part (Fig. 5(a)) shows plots of $\theta_a(z)$ and $m(z)$ vs. scan position z calculated from Eq. (4) for three cases: the air gap cell (n_{cell} = 1, purple); the planar limit LC cell at $v = 0$ (n_{cell} = 1.70, black), and the homeotropic limit LC cell at $v = 6$ V (n_{cell} = 1.54, blue). The corresponding reflectivity curves are shown in Figs. 5(b) and 5(c) with the same color coding, and plotted with the $R(v,z)$ calculated from Eqs. (2) and 4 (black in (b), white in (c)), the features of which are related to the $m(z)$ plots in (a) by the color-coded vertical lines ending in open circles. These serve to illustrate that the minima in $R(v,z)$ calculated for the planar and homeotropic limits correspond to points where the $m(z)$ trajectories cross the lines at which m is integral.

The darker shaded region in between these limits in Fig. 5(a) is the domain of $m(v,z)$ accessed by increasing the voltage applied to the cell, the white arrows indicating the direction of increasing v. Increasing v from 0 to 6 V scans $m(v,z)$ by $\delta m(v,z) \approx$ -2.5 orders near $\theta_a = 0$, and by $\delta m(v,z) \approx$ -3.1 orders near $\theta_a = 50°$. This near independence of $\delta m(v,z)$ on z makes $R(v,z)$ a quasi-periodic function of z, with very similar $R(z)$ patterns appearing with voltage differences for which $\delta m = 1$ even at intermediate voltages, for example $v = 0.83$ V, with $m(v,z)$ indicated by the solid blue circles. This is the origin of the similarity between the $R(v,z)$ progressions in the 0 V $< v <$ 0.83 V and the 2.15V $< v <$ 6.00 V ranges as noted above. The reflectivities $R(v,z)$ at the limits of these ranges, shown in Fig. 5(d), are found to be comparable at small θ_a but to differ substantially at large v and θ_a. This behavior will be discussed below with the aid of Fig. 9. Figure 5(a) also enables direct assessment of the sensitivity of the interference and electro-optic behavior to changes in refractive index (due to temperature dependence or dispersion) or to changes in gap thickness.

The cell reflectivity $R(v,z = 465\mu m)$ measured at normal incidence ($\theta_a = 0$) as a function of voltage, plotted in Fig. 5(e), exhibits interference minima at orders 24, 23, and 22 at voltages $v = 0.83$ V, 1.20 V, and 6.00 V respectively, at which voltages the measured $R(v,z)$ are very similar, as seen, for example, in Fig. 5(d). Interference maxima are found at $v = 0$ V and 2.15 V and these are also similar to each other. The 5CB cell thickness was therefore chosen such that there was an on-axis ($\theta_a = 0$) reflective maximum in the planar alignment case at $v = 0$ V and an on-axis reflective minimum in the field-induced homeotropic case at $v = 6.00$ V, the highest voltage employed. The purple curve in Fig. 5(e) shows the field-induced tilt of molecular orientation in the cell center $\psi(s = t_g/2)$ associated with the variation of the refractive index that scans $m(v,z)$.

The normalized reflectivity $N(v,z)$ data in Figs. 6 and 7 all show the rapid modulation at small θ_a due to the fringe pattern in the converging light illustrated in Fig. 2(i), and Figs. 5(b)–5(d) show that experimentally this modulation is not eliminated by normalizing $R(v,z)$ for cells by $R_{glass}(z)$, i.e., that replacement of the single piece of glass with a sandwich cell fundamentally alters the fringe pattern. Thus Eq. (4) does not describe the short-period fringes at small θ_a.

$R(v,z)$ scans in the intermediate voltage range 0.83 V $< v <$ 2.15 V, shown in Fig. 8, qualitatively reflect the variations found at high and low voltage but with distinctly shallower intensity minima at extinction. The origin of this difference is summarized in Fig. 9, in which the pattern of illumination obtained with polarized, convergent incident light, and typical sample molecular orientations in the mid-plane of the cell for several applied voltages, are sketched. Along the lens axis, the polarization P_{TB} is vertical (along x) and makes an angle $\beta(s)$ with the principal molecular orientation a distance s into the cell. At a particular θ_a, this light experiences a certain integrated phase shift upon passing through the cell depending on path length, $\beta(s)$, and the birefringence of 5CB. For light entering the lens in the x-y plane, rays entering the lens at the L and R extremities have in general different $\beta(s)$ values in the cell, $\beta_L(s)$ and $\beta_R(s)$ respectively, as indicated, where $\beta_L(s) = \beta_R(s)$ in the limits of planar ($\psi(r)$ = 0°) or field-induced homeotropic ($\psi(r)$ = 90°) orientation of the LC. For a chosen θ_a, the $\psi(r)$ = 0° and 90° director orientation conditions therefore minimize the variation in

integrated phase shift for different incident azimuthal orientations on the incoming cone of light, so that they have interference minima under the same conditions, leading to high-contrast extinction minima. For the intermediate average molecular orientations appearing at intermediate voltages (Fig. 5(e)), such as those probed in Fig. 8, the L and R optical path lengths in the cell are different from each other and from that of the T and B rays, broadening the interference minima in z.
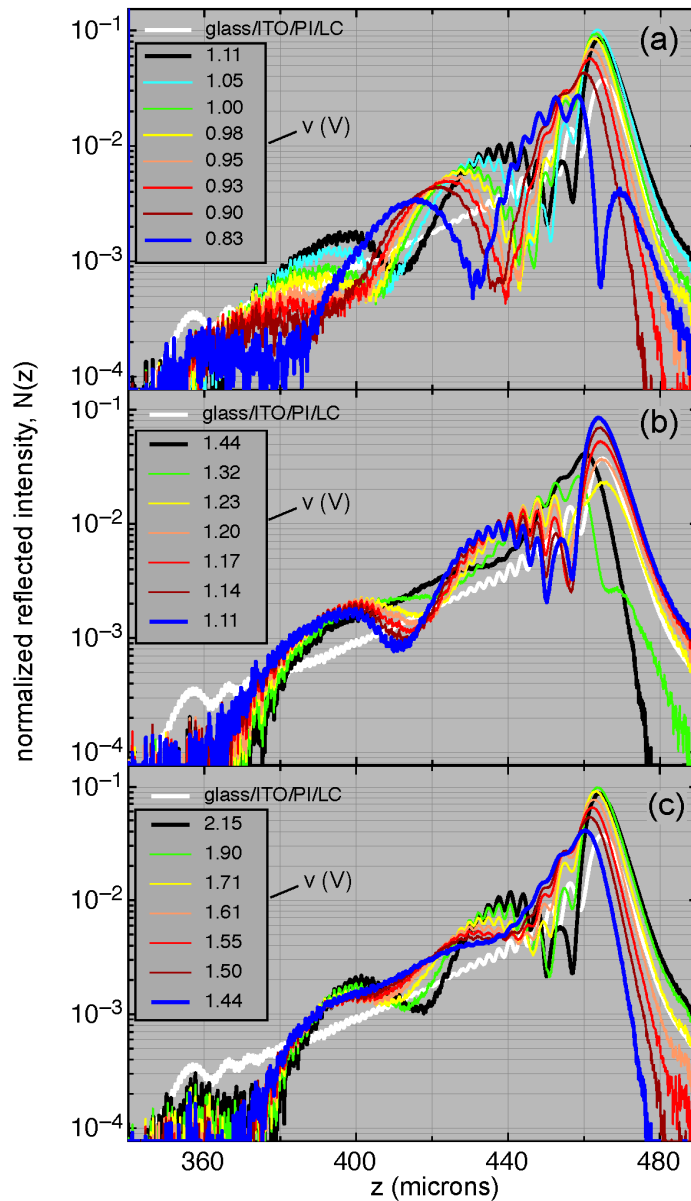

Fig. 8. (a,b) Multi-z-scan plot showing interference patterns and their voltage dependence, $N_r(z)$, for the planar aligned nematic LC 5CB cell with voltage in the intermediate range 0.83 V < v < 2.15 V. In this regime, n has a large, field-induced tilt producing different effective indices of refraction for light on opposite sides of the illumination cone, thereby shifting the extinction minima in z and reducing their contrast. Also plotted is the coated plate reflectivity $N_{coated}(z)$ including the index matching effect of the LC at $v = 0$ V (white).
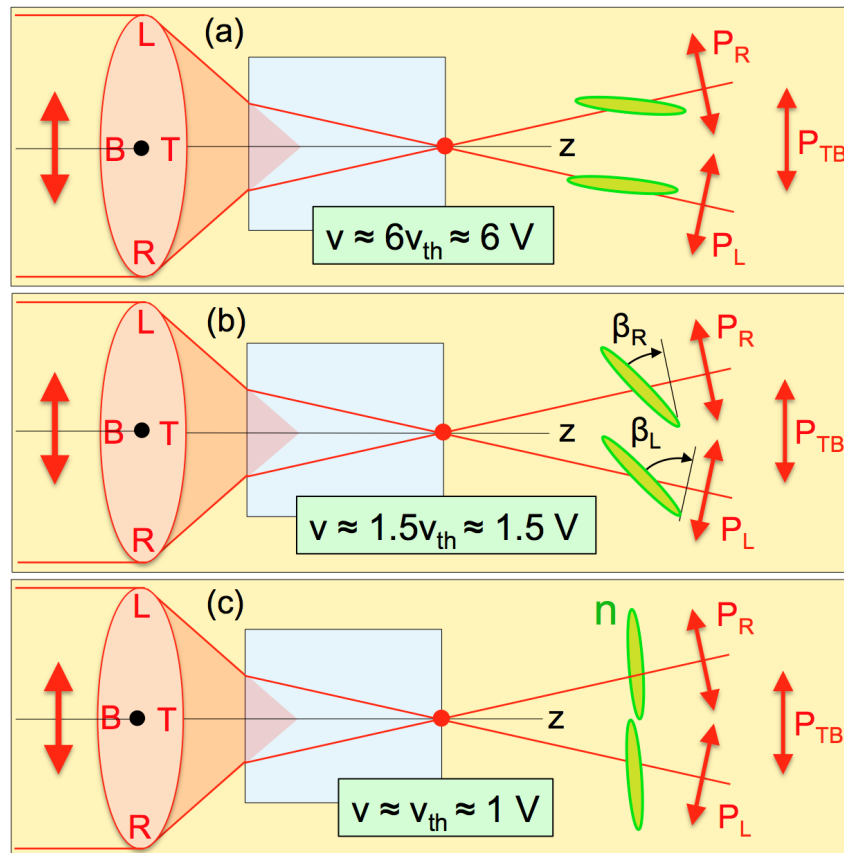
Fig. 9. Geometrical relationship between molecular orientation n at the mid-plane of the LC cell and polarization orientation for an incident parallel beam entering the objective in different quadrants (Top, Bottom, Left, Right) for several values of applied voltage v. When the applied voltage is either very large (a) or very small (c), the director field is essentially homogeneous across the cell and the distribution of polarization orientations β of the various incident rays relative to the director field n is quite narrow, so that they all experience a similar refractive index as they traverse the LC layer. The broadest distributions of polarization orientations β relative to the director field occur at intermediate voltages (b), leading to the broadest distribution of interference path differences of the rays making up the beam and the largest relative shifts of the extinction minima in z, and thus the lowest interference fringe contrast.

5. Discussion and conclusion

We have demonstrated an aberrated reflection geometry using a high numerical aperture, infinity-corrected objective that implements conical reflection with high angular resolution and precision very simply, enabling the efficient assessment of the angular dependence of the reflection of liquid crystal cells. Probing the electro-optic reflection of a planar-aligned nematic reveals a complex variation with angle of incidence and applied electric field, the basic features of which can be quantitatively understood, and shows that such a cell can exhibit high contrast electro-optic switching in conical reflection for linearly polarized light at angles of incidence up to $\theta_a \sim 30°$. With a restricted azimuthal range of the incident light, useful electro-optic contrast should be obtainable for θ_a as large as $60°$, well into the range required for retro-reflection applications. This research advances our understanding of liquid crystal remote sensing communication, suggesting a lightweight, inexpensive, and easy to employ technology that could become a workhorse in the burgeoning industry of sensors and sensing, as liquid crystals are for portable displays.

Author contributions

A.S.A. set up and carried out the experiment, analyzed the data, created figures, and wrote the manuscript; Z.N. assisted with setting up the experiment; J.E.M. edited the manuscript and contributed to the figures; N.A.C. conceived and designed the experiments, analyzed and modeled the data, and wrote the manuscript.

References

1. C. K. Kirkendall and F. Bucholtz, "Self aligning demodulator for remotely operated fiber optic magnetic sensor system," Electron. Lett. **30**(12), 999–1000 (1994).
2. M. J. Sepaniak, T. Vo-Dinh, D. L. Stokes, V. Tropina, and J. E. Dickens, "Demonstration of an integrated capillary electrophoresis-laser-induced fluorescence fiber-optic sensor," Talanta **43**(11), 1889–1901 (1996).
3. M. A. Farahani and T. Gogolla, "Spontaneous Raman scattering in optical fibers with modulated probe light for distributed temperature Raman remote sensing," J. Lightwave Technol. **17**(8), 1379–1391 (1999).
4. V. Semwal, A. M. Shrivastav, and B. D. Gupta, "Surface plasmon resonance based fiber optic trichloroacetic acid sensor utilizing layer of silver nanoparticles and chitosan doped hydrogel," Nanotechnology **28**(6), 065503 (2017).
5. G. P. Anderson, K. D. King, D. S. Cuttino, J. P. Whelan, F. S. Ligler, J. F. MacKrell, C. S. Bovais, D. K. Indyke, and R. J. Foch, "Biological agent detection with the use of an airborne biosensor," Field Anal. Chem. Technol. **3**(4-5), 307–314 (1999).
6. M. A. Geday, G. del Campo, A. Carrasco, N. Bennis, X. Quintana, F. J. López-Hernandez, and J. M. Otón, "V-Shape Liquid Crystal-Based Retromodulator Air to Ground Optical Communications," Mol. Cryst. Liq. Cryst. (Phila. Pa.) **494**(1), 213–221 (2008).
7. B. E. Bernacki, N. C. Anheier, K. Krishnaswami, B. D. Cannon, and K. B. Binkley, "Design and fabrication of efficient miniature retroreflectors for the mid- and long-range infrared," Proc. SPIE **6940**, 69400X (2008).
8. X. Jin and J. F. Holzman, "Differential retro-detection for remote sensing applications," IEEE Sens. J. **10**(12), 1875–1883 (2010).
9. B. Sandnes, T. A. Kelf, H. Liu, and A. V. Zvyagin, "Retroemission by a glass bead monolayer for high-sensitivity, long-range imaging of upconverting phosphors," Opt. Lett. **36**(15), 3009–3011 (2011).
10. P. Schultz, B. Cumby, and J. Heikenfeld, "Investigation of five types of switchable retroreflector films for enhanced visible and infrared conspicuity applications," Appl. Opt. **51**(17), 3744–3754 (2012).
11. I. Woo, S. Yu, J. S. Lee, J. H. Shin, M. Jung, and N. Park, "Plasmonic structural-color thin film with a wide reception angle and strong retro-reflectivity," IEEE Photonics J. **4**(6), 2182–2188 (2012).
12. C. C. Chang, M. C. Su, Y. C. Yang, and J. Tsai, "Design, fabrication, and characterization of tunable cat's eye retroreflector arrays as optical identification tags," J. Lightwave Technol. **32**(3), 384–391 (2014).
13. L.-X. Zhang, H.-Y. Sun, Y.-Z. Zhao, J. Yang, and Y.-H. Zheng, "Large incidence angle and defocus influence cat's eye retro-reflector," Proc. SPIE **9300**, 93000C (2014).
14. E. V. Khaydukov, V. A. Semchishen, and A. V. Zvyagin, "Incoherent wavefront reconstruction by a retroemission device," Opt. Lett. **40**(7), 1169–1172 (2015).
15. R. Mahon, M. S. Ferraro, P. G. Goetz, C. I. Moore, J. Murphy, and W. S. Rabinovich, "Irradiance correlations in retro-reflected beams," Appl. Opt. **54**(31), F96–F102 (2015).
16. W. S. Rabinovich, C. I. Moore, R. Mahon, P. G. Goetz, H. R. Burris, M. S. Ferraro, J. L. Murphy, L. M. Thomas, G. C. Gilbreath, M. Vilcheck, and M. R. Suite, "Free-space optical communications research and demonstrations at the U.S. Naval Research Laboratory," Appl. Opt. **54**(31), F189–F200 (2015).
17. S. R. Soomro and H. Urey, "Design, fabrication and characterization of transparent retro-reflective screen," Opt. Express **24**(21), 24232–24241 (2016).
18. A. Arbabi, E. Arbabi, Y. Horie, S. M. Kamali, and A. Faraon, "Planar metasurface retroreflector," Nat. Photonics **11**(7), 415–420 (2017).
19. B. Born, I. R. Hristovski, S. Geoffroy-Gagnon, and J. F. Holzman, "All-optical retro-modulation for terabit-per-second freespace optical communication," Proc. SPIE **10524**, 1052405 (2018).
20. Y. Jia, J. Wang, Y. Li, Y. Pang, J. Yang, Y. Fan, and S. Qu, "Retro-reflective metasurfaces for backscattering enhancement under oblique incidence," AIP Adv. **7**(10), 105315 (2017).

21. P. Schultz and J. Heikenfeld, "Enhanced optical discrimination system based on switchable retroreflective films," Opt. Eng. **55**, 04510 (2016).
22. S. Ikpe and G. Triplett, "Improved optical resonance in mid-infrared GaAs-based modulating retro-reflectors," Proc. SPIE **9481**, 94810A (2015).
23. S. Mathews, G. Farrell, and Y. Semenova, "Liquid crystal filled photonic crystal fibers for voltage sensing applications," Proc. SPIE **7726**, 77260R (2010).
24. S. Mathews, Y. Semenova, G. Rajan, and G. Farrell, "Experimental demonstration of a ferroelectric LC tunable filter for fast demodulation of FBG Sensors," Proc. SPIE **7356**, 73561O (2009).
25. S. Mathews, G. Farrell, and Y. Semenova, "All-fiber polarimetric electric field sensing using liquid crystal infiltrated photonic crystal fiber," Sens. Actuators A Phys. **167**(1), 54–59 (2011).
26. S. Mathews, Y. Semenova, G. Rajan, and G. Farrell, "Discretely tunable ferroelectric liquid crystal filter for demodulation of multiple FBG sensors," Proc. SPIE **7003**, 70031X (2008).
27. Objective Lenses http://www.olympus-ims.com/en/microscope/uis2/
28. S. H. Wiersma, P. Török, T. D. Visser, and P. Varga, "Comparison of different theories for focusing through a plane interface," J. Opt. Soc. Am. A **14**(7), 1482–1490 (1997).
29. J. Kim, Y. Wang, and X. Zhang, "Comparison of different theories for focusing through a plane interface: comment," J. Opt. Soc. Am. A **35**(4), 591–592 (2018).
30. S. H. Wiersma, P. Török, T. D. Visser, and P. Varga, "Comparison of different theories for focusing through a plane interface: reply," J. Opt. Soc. Am. A **35**(4), 593 (2018).
31. P. Török, P. Varga, Z. Laczik, and G. R. Booker, "Electromagnetic diffraction of light focused through a planar interface between materials of mismatched refractive indices: an integral representation," J. Opt. Soc. Am. A **12**(2), 325–332 (1995).
32. P. Török, P. Varga, Z. Laczik, and G. R. Booker, "Electromagnetic diffraction of light focused through a planar interface between materials of mismatched refractive indices: an integral representation: errata," J. Opt. Soc. Am. A **12**(2), 325–332 (1995).
33. S. H. Wiersma and T. D. Visser, "Defocusing of a converging electromagnetic wave by a plane dielectric interface," J. Opt. Soc. Am. A **13**(2), 320–325 (1996).
34. P. Török and P. Varga, "Electromagnetic diffraction of light focused through a stratified medium," Appl. Opt. **36**(11), 2305–2312 (1997).
35. P. Török, "Focusing of electromagnetic waves through a dielectric interface by lenses of finite Fresnel number," J. Opt. Soc. Am. A **15**(12), 3009–3015 (1998).
36. J. Kim, Y. Wang, and X. Zhang, "Calculation of vectorial diffraction in optical systems," J. Opt. Soc. Am. A **35**(4), 526–535 (2018).
37. P. Torok, P. Varga, and G. R. Booker, "Electromagnetic diffraction of light focused through a planar interface between materials of mismatched refractive indices: structure of the electromagnetic field. I," J. Opt. Soc. Am. A **12**(10), 2136–2144 (1995).
38. P. Török, P. Varga, A. Konkol, and G. R. Booker, "Electromagnetic diffraction of light focused through a planar interface between materials of mismatched refractive indices: structure of the electromagnetic field. II," J. Opt. Soc. Am. A **13**(11), 2232–2238 (1996).
39. C. J. R. Sheppard and P. Török, "Effects of specimen refractive index on confocal imaging," J. Microsc. **185**(3), 366–374 (1997).
40. S. H. Wiersma, T. D. Visser, and P. Török, "Focusing through an interface: scanning and localizing the intensity," Opt. Lett. **23**(6), 415–417 (1998).
41. S. H. Wiersmay, T. D. Visseryx, and P. Török, "Annular focusing through a dielectric interface: scanning and confining the intensity," Pure Appl. Opt. **7**(5), 1237–1248 (1998).
42. F. C. Frank, "I. Liquid crystals. On the theory of liquid crystals," Disc. Farad. Soc. **25**, 19 (1958).
43. P. G. de Gennes and J. Prost, *The Physics of Liquid Crystals* (Clarendon, 1993).
44. *Handbook of Liquid Crystals*, 2nd ed., edited by J.W. Goodby, P. J. Collings, T. Kato, C. Tschierske H. F. Gleeson and P. Raynes (Wiley-VCH, 2014).